Batteries Hot Paper

How to cite:
International Edition: doi.org/10.1002/anie.202102552
German Edition: doi.org/10.1002/ange.202102552

Consecutive Nucleation and Confinement Modulation towards Li Plating in Seeded Capsules for Durable Li-Metal Batteries

*Minsong Huang, Zhenguo Yao, Qifan Yang, and Chilin Li**

***Abstract:** A dual modulation strategy of consecutive nucleation and confined growth of Li metal is proposed by using the metal–organic framework (MOF) derivative hollow capsule with inbuilt lithiophilic Au or Co-O nanoparticle (NP) seeds as heterogeneous host. The seeding-induced nucleation enables the negligible overpotential and promotes the inward injection of Li mass into the abundant cavities in host, followed by the conformal plating of Li on the outer surface of host during discharging. This modulation alleviates the dendrite growth and volume expansion of Li plating. The interconnected porous host network enables enhancement of cycling and rate performances of Li metal (a lifespan over 1200 h for Au-seeding symmetric cells, and an endurance of 220 cycles under an ultrahigh current density of 10 mA cm^{-2} for corresponding asymmetric cells). The hollow capsules integrated with lithiophilic seeds solve the deformation problem of Li metal for durable and long-life Li-metal batteries.*

Introduction

Owing to the low theoretical specific capacity, graphite anode greatly limits the future application of lithium-ion batteries (LIBs) in the large-scale markets demanding high energy density. Metallic lithium (Li) has been proposed as a promising anode to achieve the high-energy storage, especially when combining with conversion-type cathodes such as sulfur, oxygen or fluorides, because of its ultrahigh theoretical specific capacity (3860 mAh g^{-1}) and the lowest redox potential (−3.04 V vs. standard hydrogen electrode).[1–3] However, the consecutive growth of Li dendrites and infinite dimension change during cycling severely restrain the practical application of Li metal anode.[4,5] Its huge deformation would lead to the increase of internal pressure and fragmentation of solid-electrolyte interphase (SEI) layer. The already generated Li dendrites would exfoliate to form "dead Li".[6–8] The accumulation of Li dendrites could even penetrate the separator and cause the hazard of cell short circuit.[9] The high-surface-area dendritic Li would also consume electrolyte and degrade the utilization of anode. These undesired factors can cause a fluctuant Coulombic efficiency (CE) and accelerate the capacity fading and failure of full cells.[10,11]

To circumvent these issues of Li metal anode, efficacious strategies have been proposed to suppress the growth of Li dendrites and thus improve the electrochemical performance of LMBs. These strategies include i) the stabilization of SEI layer via modifying the electrolyte composition and introducing electrolyte additives,[7,12–16] ii) the engineering of robust interfacial protective layer and 3D host structure,[8,10,17–22] and iii) the application of high-modulus solid and quasi-solid electrolytes to block dendritic Li growth.[23–26] Among these approaches, the tailoring of 3D anode host is of tremendous interest to modulate the Li mass growth behavior and its volume evolution. The high surface area of 3D framework enables the reduction of local current density, homogenization of electric field and restraint of charge accumulation or depletion, therefore contributing to the uniform Li-ion flux and its dendrite-less deposition.[27,28] The internal open pores of 3D framework can alleviate the volume expansion of Li plating with "hostless" nature.[29] In this regard, different 3D anode hosts such as 3D porous Cu foil,[20] Cu@Ni nanowire network[21] and 3D carbon fiber[22] have been revealed to be effective on boosting the electrochemical stability of Li metal anode. However, the intrinsically poor affinity of Li towards Cu and C leads to the evident nucleation barrier and loose attachment of Li grains, which both are detrimental to the morphology of Li deposition.[8] To this end, Cui et al. initially explored the selective Li deposition on various metal substrates with different solubility with Li.[30] They found there is no nucleation barrier for the metal having a definite solubility in Li (e.g. for Au, Mg, Zn and Ag). The resultant solid solution (or Li-contained alloy) interlayer on metal surface can act as a buffer layer for the following kinetically favorable Li plating. The deposition of Li can be spatially confined over these pre-planted lithiophilic seed positions. They then loaded these lithiophilic seeds into hollow carbon spheres by sacrificial template method for better spatial confinement effect of Li mass. However the extra etching step by strong corrodent (e.g. HF) may concurrently remove a part of metallic seeds, resulting in the diluting of lithiophilic sites and confinement degradation of this carbon host. Afterwards, Yang et al. prepared the carbonized metal-organic frameworks (MOFs) harnessed with abundant Zn clusters as lithiophilic host, and Hu et al. synthesized that the carbon

---

[*] M. Huang, Z. Yao, Q. Yang, Prof. C. Li
State Key Laboratory of High Performance Ceramics and Superfine Microstructure, Shanghai Institute of Ceramics
Chinese Academy of Sciences
585 He Shuo Road, Shanghai 201899 (China)
and
Center of Materials Science and Optoelectronics Engineering,
University of Chinese Academy of Sciences
Beijing 100049 (China)
E-mail: chilinli@mail.sic.ac.cn
M. Huang, Q. Yang, Prof. C. Li
CAS Key Laboratory of Materials for Energy Conversion
Shanghai Institute of Ceramics, Chinese Academy of Sciences
Shanghai 201899 (China)

Supporting information and the ORCID identification number(s) for the author(s) of this article can be found under: https://doi.org/10.1002/anie.202102552.

nanofibers anchored with ultrafine Ag nanoparticles via rapid Joule heating method as lithiophilic network.[27,28] However these Zn or Ag seeds are exposed on the outer surface of carbon skeleton, which has no extra confinement effect on the nucleated Li compared with hollow structure.

It is still a challenge to design the 3D anode host with the integration of lithiophilic nanoseeds into hollow structure. Herein we present a mild etching of Au-loaded MOF by tannic acid (TA) followed by carbonization to prepare hollow carbon hosts harnessed with rich lithiophilic Au nanoparticles (NPs) or etching of Co-bonded MOF by TA to prepare metal-phenolic hollow framework embedded with cobalt oxide NPs, denoted as c-Au@ZIF-8 and TA-ZIF-67, which are expected to enable the consecutive nucleation and confinement modulation towards Li plating (Figure 1 a and b). The built-in lithiophilic NP seeds can induce Li^+ to nucleate inside the host cavity with low nucleation barrier. The following Li growth is still confined by the cavity shape. Such a dual modulation of early Li growth is favorable for the later Li plating behavior with homogeneous and compact mass distribution on electrodes, compared with the single modulation only by lithiophilic site or hollow structure as already reported.[6,22] Au NPs have definite solubility in Li according to the Li-Au phase diagram (Supporting Information, Figure S1), and the cobalt oxide can also react with Li on basis of the Li-O-Co ternary phase diagram (Figure S2). Both of them can behave as pre-planted seeds to induce Li nucleation with negligible nucleation overpotential. There are two lithiation plateaus around 360 mV and about 150 mV in the discharge curve of c-Au@ZIF-8 electrode before Li nucleation (Figure 1 c), indicating the formation of at least two alloy phases of Li_xAu. Both the hollow host frameworks with superior wettability towards Li would offer sufficient interspace to accommodate Li and substantially alleviate the volume change of “hostless” Li. The enrichment of alloyable or bondable seeds and mesopores could reduce local current density and homogenize Li-ion flux and electric field distribution. Without the seeding on Cu foil, the Li deposition is prone to form dendrites with high nucleation overpotential of 138 mV (Figure 1 d). Benefiting from the synergistic effect of heterogeneous seeding and spatial confinement, this advanced structure endows the anode of LMBs with dendrite-free deposition mode, better cycling stability and endurability.

Results and Discussion

To synthesize the Au-loaded hollow MOF, a core–shell structured material with Au NPs encapsulated in zeolitic imidazolate framework-8 (Au@ZIF-8) was applied as precursor. Initially, the polyhedral Au@ZIF-8 was prepared from the poly(vinylpyrrolidone) (PVP) stabilized Au NPs and ZIF-8 precursor reagents (2-methylimidazole and $Zn(NO_3)_2$) according to the literature procedure as illustrated in Figure 2 a.[31] The Au NPs can act as seeds and facilitate the heterogeneous nucleation of ZIF-8 on their surface.[32] Subsequently, the obtained Au@ZIF-8 particles were chemically etched in TA solution via synergistic interaction between MOFs and polyphenols to construct hollow core–shell structure. These etched Au@ZIF-8 particles were then pyrolyzed at 800 °C to generate the hollow carbon capsules (i.e. c-Au@ZIF-8). The self-etching ability of TA promotes the creation of voids inside MOFs. In principle, TA molecules can conformally adsorb to the exterior surface of MOFs with the formation of metal-phenolic frameworks because of the metal-chelation ability of polyphenol.[33,34] The coordination of TA with metal nodes would break up and replace the original Zn-organic linkers.[34,35] The adsorbed TA molecules can partially block the external surface or channels of Au@ZIF-8, thus preventing the further diffusion of TA inside Au@ZIF-8 and its deeper etching towards MOFs.[36] In addition, TA as weak organic acid can continuously release free protons. The binding of TA with Zn^{2+} ions can convert the surface of MOFs from hydrophobic to hydrophilic one. These two factors synergistically allow the protons to penetrate into Au@ZIF-8 particles to progressively destroy the interior framework of Au@ZIF-8.[33,36] Although the penetration of TA molecules is retarded, the released protons undertake the following etching task to expand the hollow space. Finally, the 3D hollow structure with built-in Au nanoseeds is obtained. Crucially, the robust exterior metal-phenolic shell can protect MOFs from fully collapsing.[33]

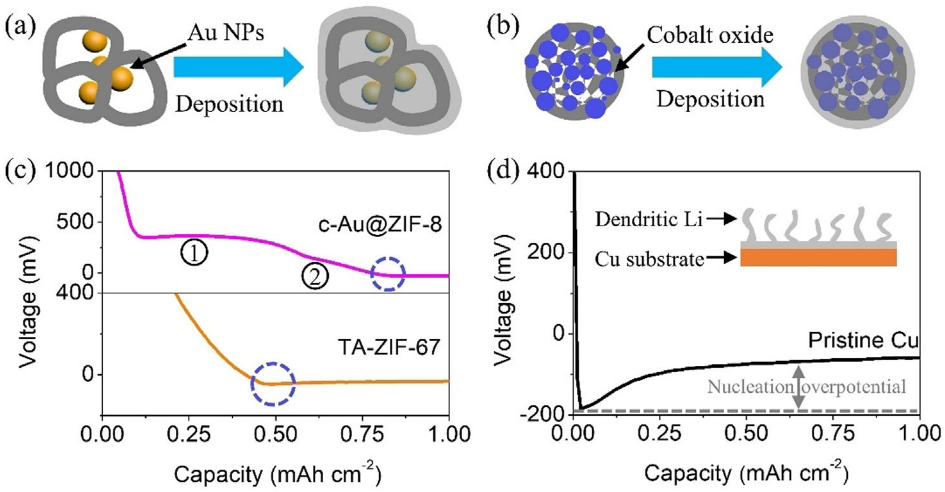

Figure 1. Li electroplating on 3D hollow a) c-Au@ZIF-8 and b) TA-ZIF-67 host based electrodes. c) Initial voltage-capacity profile of Li deposition on c-Au@ZIF-8 and TA-ZIF-67 electrodes at 1 mA cm^{-2}. d) Initial Li plating curve for pristine Cu electrode at 1 mA cm^{-2}, inset: Li dendrites on pristine Cu electrode.

The X-ray diffraction (XRD) pattern confirms that the Au@ZIF-8 precursor is composed of Au and ZIF-8 (Figure S3). The multiple diffraction signals in the 2θ range of 10–60° are attributed to ZIF-8, matching well with its simulated pattern.[37] The diffraction

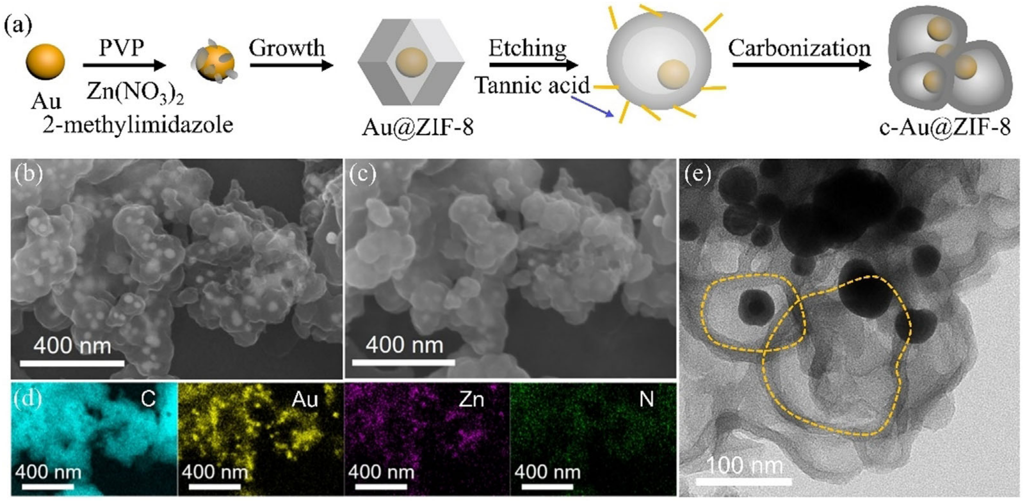

Figure 2. a) Illustration of synthesis process of hollow c-Au@ZIF-8. b) Backscattered electron image and c) surface SEM image of c-Au@ZIF-8. d) Corresponding EDS mapping of C, Au, Zn, and N element distribution in c-Au@ZIF-8. e) TEM image of c-Au@ZIF-8 with the appearance of core–shell structure.

peaks at 38.2°, 44.4°, 64.6° and 77.5° are assigned to Au (111), (200), (220) and (222), respectively. After calcination, only the peaks of Au are observed in c-Au@ZIF-8 sample and the metal-phenolic frameworks are pyrolyzed into amorphous carbon. The morphology and structure of Au@ZIF-8 are characterized by scanning electron microscopy (SEM) and transmission electron microscopy (TEM) as shown in Figure S4. The Au@ZIF-8 grains have the size around 250 nm and polyhedral geometry. These grains are linked by sharing their edges and facets, which is favorable for the formation of carbon framework network after pyrolysis with the inheritance of precursor morphology. One can note that the surface of polyhedra is porous, and it enables the better adsorption and penetration of TA etching agent. From the higher-resolution TEM, the encapsulated Au seeds with a uniform size around 30 nm and excellent dispersity are observed. The rich grain boundaries in ZIF-8 guarantee the sufficient etching process by TA molecules. After the following etching and carbonization processes, the polyhedral Au@ZIF-8 particles evolve into a 3D interconnected network of Au-C core–shell hollow structures (i.e. c-Au@ZIF-8, Figure 2b). The energy dispersive X-ray spectroscopy (EDS, Figure 2c and d) mapping confirms the coexistence of C, Au, Zn and N elements in c-Au@ZIF-8. Note that Zn element has the similar spatial distribution as that of Au, indicating that some residual Zn may be adsorbed on the surface of Au NPs to form an alloy phase.[38] The content of Zn (2.49 wt%, according to EDS) is much less than that of Au (27.80 wt%), because most of Zn^{2+} ions are released into the solution after the Zn-imidazolate coordination bonds are broken by TA. The most adjacent Zn^{2+} ions (to Au surface) are not etched off and left to alloy with Au NPs. The EDS result indicates that the much fewer Zn atoms do not produce excess lithiophilic domains apart from the Au dominated zones. These residual Zn atoms are expected to reinforce the lithiophilic nature of seeds and decrease the nucleation barrier of Li plating.[27] The detectable N element residual is also beneficial to the lithiophilic effect of carbon framework.[6,39] The hollow structure with the encapsulation of Au NPs can be more clearly disclosed in the TEM imaging of Figure 2e.

The initial Li deposition onto c-Au@ZIF-8 and pristine Cu substrates at 1 mA cm^{-2} is characterized by SEM imaging to gain insight into the nucleation and growth behaviors of Li metal. The plated Li on pristine Cu foil is loosened and rough with visible Li dendrites under a plating capacity of 2 mAh cm^{-2} (Figure 3a and b). These Li dendrites are prone to peel off from the substrate during the cross-section sample preparation. The irregular sharped dendrites are inclined to impale separator and accelerate the degradation of CE. The prevailing of vertical dendrites leads to a thick Li plating of about 12–13 μm in thickness. In the case of c-Au@ZIF-8 substrate, the top surface and cross section are comparatively more compact and smoother without the creation of dendritic Li (Figure 3c and d). This Li plating is confined in a much thinner thickness of 6–8 μm with firm planting on c-Au@ZIF-8. Therein the synergistic effect of lithiophilic Au NPs and hollow 3D core–shell structure are expected to regulate the uniform deposition of Li and its dendrite suppression. This modulation effect could be further demonstrated by the cross-sectional SEM images of initial Li deposition with a smaller capacity of 0.5 mAh cm^{-2}. As illustrated in Figure 3e, the deliberatively chosen backscattered electron image exhibits the clear distribution of Au NPs. The pre-planted Au seeds can serve as preferential nucleation sites for Li deposition. Thus, it is found that Li metal species more sufficiently grows around the Au NPs due to the zero nucleation overpotential (Figure 3f). The elimination of nucleation barrier is attributed to the solubility (or alloyability) of Li in Au. Note that the deposited Li is diluted in the area with fewer Au NPs. Under this areal capacity, the original morphology of c-Au@ZIF-8 host is well preserved, as most of plated Li is injected into the hollow structure and Li plating does not accumulate on the outer surface of decoration layer (Figure 3g). We also observe the stuffed Li without the dendrite morphology near the Au NPs in the magnified SEM image

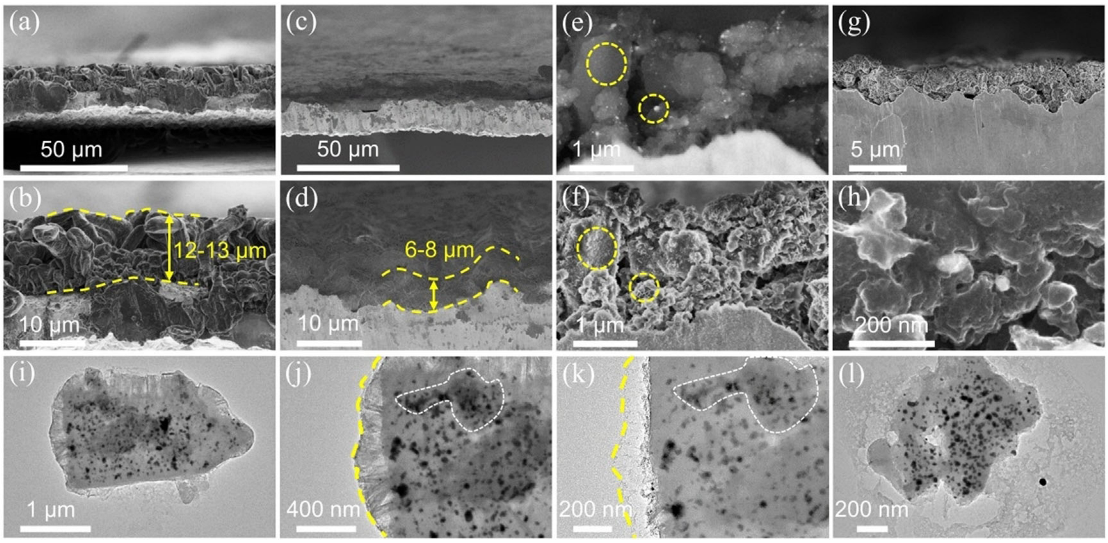

Figure 3. Cross-sectional morphologies of Li plating on a,b) pristine Cu and c,d) c-Au@ZIF-8 electrodes with a plating capacity of 2 $\mathrm{mAh\,cm^{-2}}$ at 1 $\mathrm{mA\,cm^{-2}}$. e) Backscattered and f) corresponding cross-sectional SEM images of Li plating on c-Au@ZIF-8 electrode with a small plating capacity of 0.5 $\mathrm{mAh\,cm^{-2}}$ at 1 $\mathrm{mA\,cm^{-2}}$. g) Low-magnification SEM image of Li deposition on c-Au@ZIF-8 electrode with a capacity of 0.5 $\mathrm{mAh\,cm^{-2}}$ and h) magnified SEM image of Li deposit around Au NPs. TEM images of lithiated c-Au@ZIF-8 (i,j) before and (k) after high energy e-beam irradiation. l) TEM image of lithiated c-Au@ZIF-8 in the process of Li melting.

(Figure 3h). Actually when increasing the lithiation capacity from 0.5 to 2 $\mathrm{mAh\,cm^{-2}}$, the Li plating thickness does not remarkably increase (merely from 5 to 6–8 μm) in view of the consecutive modulation of nucleation and confinement. It appears that the plated Li progressively infills the nanopores of c-Au@-ZIF-8 host and then the voids between host particles, thus achieving the highly dense Li deposition without dendrite prevailing.

The TEM images (Figure 3i–k) further verify that the lithiophilic c-Au@-ZIF-8 could spatially guide Li nucleation within the hollow core–shell structure. After galvanostatic deposition with an areal capacity of 2 $\mathrm{mAh\,cm^{-2}}$, one can note that there is a translucent Li layer of 200–400 nm thickness planted on the whole surface of c-Au@-ZIF-8 host. The translucent layer consists of many columnar structures based on the island-like growth mode (Figure 3i and j). After the high energy e-beam irradiation for 5 s (Figure 3k), this external Li layer fleetly melts and sublimates in the same observation zone. This phenomenon further confirms the successful TEM observation of Li metal plating, which is significant to disclose the texture information of metallic Li depending on substrate and host properties. In the meantime, the area around Au NPs inside c-Au@-ZIF-8 is more lightly colored under irradiation, indicating that the Li metal has entered into the hollow structure and nucleated around these lithiophilic seeds. Under the stronger irradiation, we capture an image of Li metal in the process of melting as shown in Figure 3l. It is obviously observed that the superficial Li and the internal Li around broken carbon shell simultaneously disappear. These TEM results well confirm the selective Li deposition induced by lithiophilic Au seeds and hollow host.

To validate the effectiveness of c-Au@-ZIF-8 structure, galvanostatic cycling measurement was performed in symmetric cells at 1 $\mathrm{mA\,cm^{-2}}$ with a capacity of 2 $\mathrm{mAh\,cm^{-2}}$. The Li plating of 5 $\mathrm{mAh\,cm^{-2}}$ is preloaded on the c-Au@-ZIF-8 electrode prior to cycling. As shown in Figure 4a, the symmetric cell with pristine Li anodes exhibits the high voltage gap of ca. 40 mV between plating and stripping plateaus. A sudden drop in voltage shows up merely after 260 h, indicative of the prevailing of dendritic Li and occurrence of internal short-circuit. Benefiting from the modified nucleation process and lessened local current density by lithiophilic 3D frameworks, the symmetric cell with lithiated c-Au@-ZIF-8 electrodes shows much lowered voltage gap of ca. 22 mV and highly stable long-term cycle performance for at least 1200 h. Note that the c-Au@-ZIF-8 decoration enables the quite flat and stable plateaus without peaking or arching voltage traces, confirming the facile nucleation and uniform growth of Li in c-Au@-ZIF-8 with smooth charge and mass transport.

CE is defined as the ratio of Li stripping capacity to plating capacity for each cycle, and it provides another indicator of electrochemical stability of Li metal anode upon repeated cycles.[10,40] Figure 4b–e compare the cycling retention of CE and voltage hysteresis (VH) based on different electrodes at different current densities. The latter is determined by the difference between the Li stripping and plating voltage plateaus in Li/Cu asymmetric cells.[7] Therein the Li with a constant amount of 1 $\mathrm{mAh\,cm^{-2}}$ is deposited on corresponding working substrate, which is then charged to 1 V (vs. $\mathrm{Li/Li^{+}}$) to strip the deposited Li. When the Li/Cu cells are tested at a high current density of 3 $\mathrm{mAh\,cm^{-2}}$, the CE value for bare Cu foil declines rapidly after 90 cycles, while the cell based on c-Au@ZIF-8 electrode enables a retention of high CE value (>98%) over 330 cycles (Figure 4b). To further emphasize the superiority of seeded hollow host, we also investigated the cycling stability of carbonized hollow ZIF-8 (c-ZIF-8) without the loading of Au nanoseeds. Its CE drops below 90% after 190 cycles. This cycling performance is better than that for pristine Cu foil and but worse than for c-

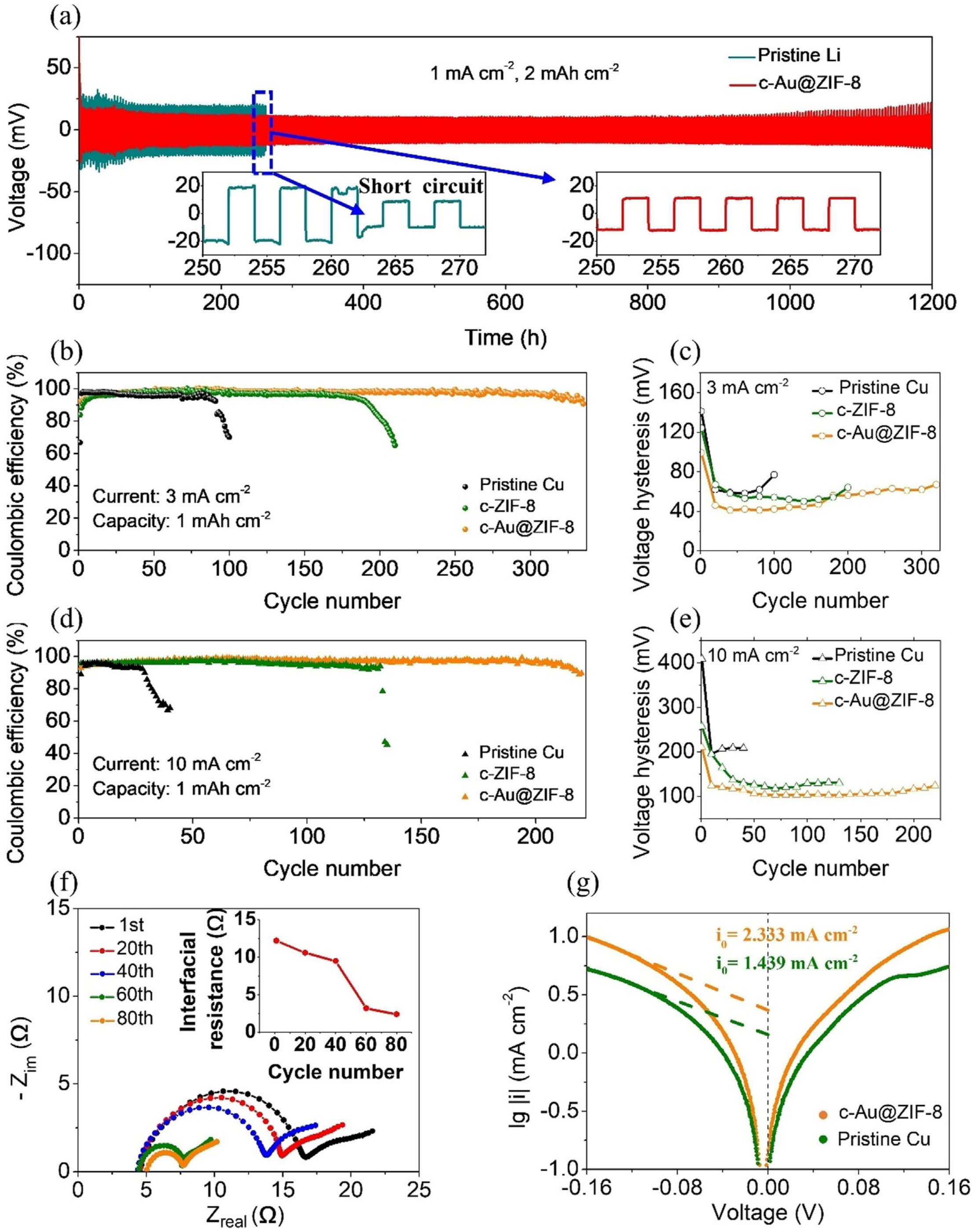

Figure 4. a) Electrochemical performance of symmetric cells with lithiated c-Au@ZIF-8 and pristine Li foil electrodes at 1 mA cm^{-2}, insets: corresponding voltage profiles around 260 h. Comparison of coulombic efficiencies of Li/Cu asymmetric cells with pristine Cu, c-ZIF-8 and c-Au@ZIF-8 electrodes at b) 3 mA cm^{-2} and d) 10 mA cm^{-2}. Corresponding voltage hysteresis as a function of cycle number at c) 3 mA cm^{-2} and e) 10 mA cm^{-2}. f) Impedance spectra of c-Au@ZIF-8 based on asymmetric cell at different cycle stages at 1 mA cm^{-2}, inset: evolution of corresponding interface resistances as a function of cycle number. g) Tafel curves of c-Au@ZIF-8 and Cu electrodes to evaluate their exchange current densities.

Au@-ZIF-8 electrode. The VH values for all three substrates reduce at the initial stage, attributing to the electrode activation process and the formation of desired SEI layer.[41] Unsurprisingly, the c-Au@ZIF-8 based cell shows the lowest VH (ca. 40 mV) at the early stage, which slightly increases to 63 mV after 240 cycles (Figure 4c). In contrast, the VH values for c-ZIF-8 and pristine Cu electrodes are 55 mV and 60 mV respectively, and they then increase to 65 mV and 77 mV after 190 and 90 cycles, respectively. To test the tolerability on current density, we further increase the current density to much higher 10 mA cm^{-2}. In sharp contrast, the c-Au@ZIF-8 electrode can still maintain the fantastic cycle ability for

220 cycles with a high CE of 98 %, whereas the effective cycling can be only performed for short 30 cycles for pristine Cu electrode (Figure 4 d). The c-ZIF-8 electrode also exhibits a quick CE drop after 130 cycles. As shown in Figure 4 e, for c-Au@ZIF-8 electrode a lower VH of ca. 100 mV is still preserved even at ultrahigh current density. However, the VH values for c-ZIF-8 and Cu electrodes are degraded to ca. 130 and ca. 210 mV, respectively. When applying a decreased current density (1 mA cm^{-2}) but with double areal capacity (2 mAh cm^{-2}), the c-Au@ZIF-8 electrode still shows the cycling superiority (Figure S5a). Although all the electrodes enable a high CE value of 99 %, the CE values for the bare Cu and c-ZIF-8 electrodes sharply decay after 100 and 200 cycles, respectively. Such an early CE degradation implies the pernicious Li deposition and uncontrollable Li dendrite growth especially when the Li plating is thickened. In contrast, the Li deposition behavior is better regulated in the 3D hollow c-Au@-ZIF-8 electrode, as reflected by the much stable CE over 430 cycles. Correspondingly, the VH value (ca. 23 mV) for c-Au@-ZIF-8 electrode enables the less fluctuation over 350 cycles (Figure S5b). But the VHs for c-ZIF-8 and bare Cu electrodes increase to 30 and 43 mV after 200 and 100 cycles, respectively. Additionally, we also trace the nucleation overpotential (11 mV) for c-ZIF-8 during Li plating at 1 mA cm^{-2} (Figure S6). The etching of Zn atoms is responsible for the existence of nucleation barrier. Therefore the extraneous imposition of lithiophilic seeds is crucial to eliminate the nucleation overpotential as seen in the case of c-Au@-ZIF-8 (Figure 1 c). The larger nucleation overpotential is highly associated with the worse anode performance. These results jointly prove the synergistic effect of heterogeneous nano-seeding and 3D hollow framework on the longer lifespan and more confined deposition behavior.

To validate the charge-transfer advantage of c-Au@ZIF-8 electrode, electrochemical impedance spectroscopy (EIS) was conducted on the asymmetric cell incorporating the pre-lithiated c-Au@ZIF-8 or pristine Cu electrode. As shown in Figure 4 f, The Nyquist plots for cycled and plated c-Au@ZIF-8 electrodes display one high-frequency semicircle denoting the interfacial resistance (R_i), which contains the coupled contributions from SEI layer and charge-transfer resistances.[3] The R_i value is as low as 12.2 Ω after the first cycle, which is much smaller than that for bare Cu electrode at the corresponding cycling stage (37.3 Ω, Figure S7a). The inferior affinity of Cu to plated Li is responsible for the more resistant interface and prejudicial interfacial kinetics, as indicated by the larger voltage polarization in symmetric and asymmetric cells. After 20 cycles, the R_i value for lithiated c-Au@ZIF-8 is 10.6 Ω, still lower than that for lithiated pure Cu (22.3 Ω). For the former, the R_i value decreases gradually with the progress of cycling and further shrinks to as small as 2.4 Ω after 80 cycles, in view of the optimization of confinement effect of Li plating during cycling without serious thickening of insulating SEI. By contrast, the high nucleation barrier on bare Cu electrode triggers the popularization of dendritic and dead Li regions and therefore thick accumulation of SEI even after first plating. The interfacial resistance is still as high as 16.6 Ω after 80 cycles. The kinetic advantage of c-Au@ZIF-8 substrate is further demonstrated by the exchange current density (I_0, Figure 4 g), which is calculated from Tafel plots of symmetric cell derived from linear sweep voltammetry (LSV, Figure S7b). The I_0 value for c-Au@ZIF-8 reaches to 2.333 mA cm^{-2}, whereas it is much lower for pristine Cu electrode (1.439 mA cm^{-2}). Higher I_0 value enables a faster charge transfer across the hollow conductive network filled with confined Li.

The seeding-induced Li deposition can not only be regulated by alloyable metals (Au, Ag, Zn),[27,28,30] but also is expected to be extended to conversion-type metal oxides.[42] To elucidate the feasibility of conversion nanoseeds to guide Li nucleation, we synthesized 3D porous ZIF-67 capsules harnessed with cobalt oxide NPs also through polyphenol etch but with the addition of ethanol to control the etching degree. As illustrated in Figure 5 a, ZIF-67 particles are etched into TA solution for 10 min on the basis of synergistic interaction between MOFs and TA. They are converted into interconnected hollow structure embedded with cobalt oxide NPs (denoted as TA-ZIF-67). The crystal structures and morphologies of the resultants before and after etching are characterized by XRD, SEM and TEM. The diffraction profile of ZIF-67 is in line with its simulated pattern (Figure S8).[43] However, after etching process, no diffraction peaks are clearly observed in TA-ZIF-67 and the peaks of original ZIF-67 disappear (Figure 5 b), indicating the amorphous nature of etched resultant. The primary ZIF-67 has a polyhedron shape with a diameter of ca. 350 nm (Figure 5 c and d), whereas the etching process morphs them from rhombic dodecahedra into sphere due to the anisotropic etching by TA (Figure 5 e and f).[44] From TEM imaging, the internal metal nodes are interrupted after etching and numerous nanoparticles (30–50 nm) are formed inside TA-ZIF-67 capsule (Figure 5 g). This etch-induced grinding effect leaves sufficient space to accommodate Li in these capsules, which have much larger size (500–700 nm) than that of ZIF-67 precursor. The metal-phenolic interaction at ZIF-67 surface drives the outward diffusion and run-off of Co and therefore the internal dilution of node and ligand species. This force is responsible for the volume expansion of capsule with metal-phenolic shell. The concentration of Co-contained nanodomains with high dispersity is also clearly indicated from the bright contrast in backscattered electron image (Figure S9a). The EDS mapping further shows the homogeneous distribution of C, Co and O elements throughout TA-ZIF-67 particles (Figure S9b and c). The linear scanning across one NP discloses that both Co and O have the similar distribution pattern with higher element content at the position of NP (Figure S9d). Therefore, it is reasonable to ascribe these NPs to Co-O clusters or amorphous cobalt oxide. The limited etching by TA as chelating agent and proton source leads to the residual of Co-O seeds without serious compromise of hollow host.

To confirm the chemical state of embedded NPs, TA-ZIF-67 is pyrolyzed at 800 °C (denoted as c-TA-ZIF-67) as a comparison. c-TA-ZIF-67 displays the distinct XRD peaks corresponding to metallic Co (Figure 5 b). It is imaginable that Co-O species can be thermally reduced to abundant Co nanoparticles surrounded carbonization framework (Figure S10a). Note that the carbonization process triggers the

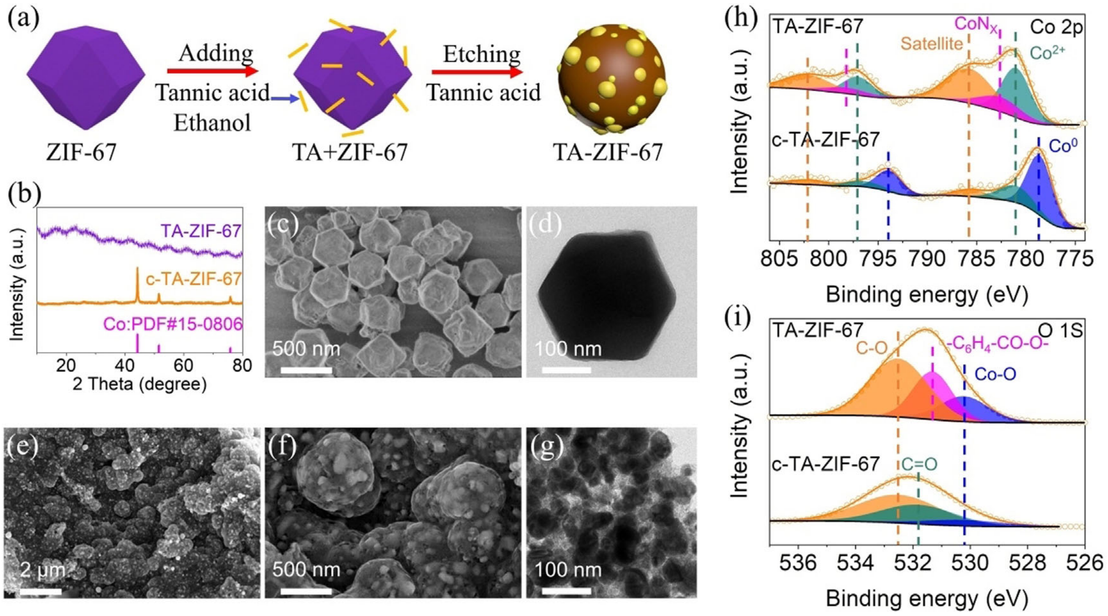

Figure 5. a) Illustration of etching process on ZIF-67 by tannic acid to obtain 3D porous TA-ZIF-67. b) XRD patterns of TA-ZIF-67 and c-TA-ZIF-67. c) SEM and d) TEM images of pristine ZIF-67 before etching. e,f) SEM and g) TEM images of TA-ZIF-67 after etching in different scales. High-resolution XPS spectra of h) Co 2p and i) O 1s for TA-ZIF-67 and c-TA-ZIF-67 samples.

collapse of capsule and hollow structures. The internal pore volume shrinks especially in the regions around Co NPs (Figure S10b). The potential catalysis of Co atoms at high temperature may be also responsible for the degradation and densification of capsules.[45] X-ray photoelectron spectroscopy (XPS) analysis was performed to detect the resultants before and after carbonization. Both the survey XPS spectra show the presence of C, N, O, and Co elements in TA-ZIF-67 and c-TA-ZIF-67 samples (Figure S11). Accordingly, the O content decreases and C content increases after carbonization. In the C 1s spectrum of TA-ZIF-67, there are three peaks located at 284.8, 286.5 and 288.6 eV, corresponding to C−C, C−O and -C_6H_4-CO-O, respectively, indicating the conjugation TA molecules on MOFs (Figure S12a).[46] After carbonization, the peak at 288.6 eV disappears and a new peak is found at the binding energy of 289.4 eV attributed to C=O.[47,48] The N 1s spectrum of TA-ZIF-67 consists of two weak peaks centered at 399.1 and 400 eV, respectively corresponding to Co-N_x and N-H,[47] whereas that of c-TA-ZIF-67 is further weakened and it can be deconvoluted into pyridinic-N (398.7 eV), pyrrolic-N (400.2 eV) and graphitic-N (402 eV) (Figure S12b).[49] In the Co 2p spectra in Figure 5h, there are two core-level signals located at 781.4 and 797.1 eV in TA-ZIF-67, assigned to Co $2p_{3/2}$ and Co $2p_{1/2}$ respectively. The energy difference between both the peaks is about 15.7 eV, indicating the existence of Co^{2+} from cobalt oxide.[50] After deconvolution, the region of Co $2p_{3/2}$ is fitted into three peaks, respectively corresponding to Co^{2+} (780.9 eV), Co-N_x (782.5 eV) and satellite (785.6 eV) ones.[50–52] In contrast, that of c-TA-ZIF-67 is deconvoluted to Co, Co^{2+} and satellite peaks located at 778.5, 780.9 and 785.6 eV, respectively.[50,52] The residual of Co^{2+} in c-TA-ZIF-67 might originate from the superficial cobalt oxide due to the sensitivity of Co to air. The high-resolution O 1s spectrum (Figure 5i) of TA-ZIF-67 presents three chemical signals, Co-O at 530.2 eV, -C_6H_4-CO-O at 531.3 eV, and C-O at 532.5 eV, matching well with the relative intensity of corresponding assignment in C 1s and Co 2p spectra.[46,48] After carbonization, the Co-O (530.2 eV) and C-O (532.5 eV) peaks are weakened, and a different peak corresponding to C=O appears at 531.8 eV.[48] All the results clearly confirm the enrichment of Co-O clusters in amorphous NPs, which can serve as conversion-type seeds for facile Li nucleation (Figure S13).

To emphasize the lithiophility and confinement advantages of TA-ZIF-67, the performances of Li nucleation and plating on TA-ZIF-67 and c-TA-ZIF-67 electrodes are compared. The nucleation overpotential for c-TA-ZIF-67 is 33 mV (Figure S14), much higher than that of TA-ZIF-67. The reduction of Co cation and lithiophilic groups containing O and N increases the nucleation barrier on c-TA-ZIF-67. Similar to the case of c-Au@ZIF-8, the symmetric cell was performed to prove the cycling advantage of TA-ZIF-67 pre-electroplated with Li of 5 $mAh\,cm^{-2}$ (Figure 6a). Under the protocol of 1 $mA\,cm^{-2}$ and 2 $mAh\,cm^{-2}$, the cell based on lithiated TA-ZIF-67 capsule exhibits a superior cycling stability over 800 h with a quite narrow voltage gap of 23 mV. The voltage plateaus remain flat even after long-term cycling, benefiting from the facile nucleation induced by Co-O nanoseeds and Li plating confinement by capsule structure. The anode reversibility of TA-ZIF-67 is also verified in Li/Cu asymmetric cells at different current densities up to ultrahigh 10 $mA\,cm^{-2}$ (Figure 6b and c). The TA-ZIF-67 capsules enable the stable cycling performance with high CEs and low VHs for 340 and 150 cycles at 3 and 10 $mA\,cm^{-2}$ respectively (Figure S15). Therein the corresponding VH values are suppressed to ca. 45 mV and ca. 100 mV respectively. However the c-TA-ZIF-67 based cells suffer from decay of CEs merely after 170 and 110 cycles at 3 and

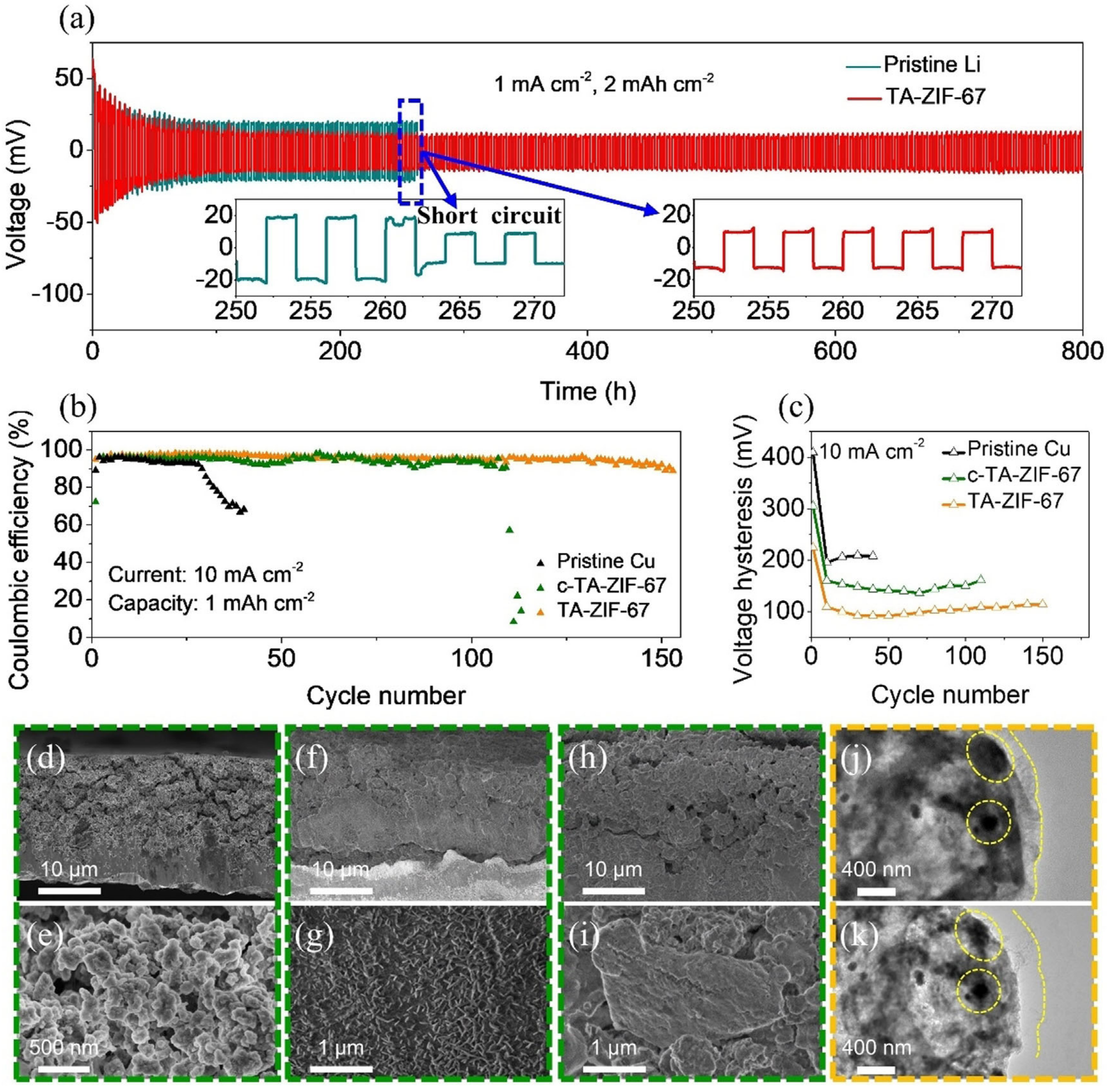

Figure 6. a) Galvanostatic cycling of symmetric cells with TA-ZIF-67 and pristine Li foil electrodes at 1 mA cm^{-2}, insets: corresponding voltage profiles around 260 h. b) Coulombic efficiencies of pristine Cu, TA-ZIF-67 and c-TA-ZIF-67 based on asymmetric cells at 10 mA cm^{-2}. c) Corresponding voltage hysteresis of different electrode as a function of cycle number at 10 mA cm^{-2}. Cross section SEM images of Li plating on TA-ZIF-67 electrode with a plating capacity of d,e) 0.5 mAh cm^{-2} and f,g) 2 mAh cm^{-2} at 1 mA cm^{-2} after initial plating. h,i) SEM images of deposited Li on TA-ZIF-67 with a capacity of 2 mAh cm^{-2} at 1 mA cm^{-2} after 40 cycles. TEM images of lithiated TA-ZIF-67 j) before and k) after high energy e-beam irradiation.

10 mA cm^{-2}, respectively. According to the binary phase diagram between Li and Co (Figure S16), Li would not react with Co to form alloy phase and there is no solubility zone of Li in metal Co, indicating the poor affinity of Co to Li. Therefore the lithiophility of c-TA-ZIF-67 is seriously degrades. Furthermore, its spatial confinement effect also degrades simultaneously due to structure densification during carbonation. The much better CE and VH endurance for TA-ZIF-67 substrate once more testify the advantage of consecutive nucleation and confinement modulation mode on Li deposition within the 3D porous lithiophilic host. Figure S17 compares the interfacial resistances (R_i) of asymmetric cells based on different substrates at different cycle stages. The R_i values for TA-ZIF-67 roughly lie between those for c-Au@ZIF-8 and bare Cu electrodes, agreeing with their electrochemical performance comparison. The exchange current density (1.829 mA cm^{-2}) for TA-ZIF-67 is correspondingly higher than that of pristine Cu, and lower than for c-Au@ZIF-8 (Figure S18), demonstrating the fast charge-transfer process in TA-ZIF-67 following the conversion reaction between cobalt oxide and Li.

The electrochemical improvement for TA-ZIF-67 is highly associated with its confinement deposition mode. After the deposition with a small capacity of 0.5 mAh cm^{-2}, the TA-ZIF-67 capsule layer is not be stuffed and its granular morphology is still visible from the cross section SEM image (Figure 6 d). Taking a close look, these Li deposits are prone to conformally wrap the surfaces of capsules after their hollow inners are preferentially filled (Figure 6 e). This deposition mode is very similar to the case of c-Au@ZIF-8, and avoids the accumulation of dendritic Li at the outer layer. The early conformal plating of Li is favorable for its deeper infiltration in capsule sublayer and therefore the volume suppression of TA-ZIF-67 coating even when increasing the Li plating capacity to much higher 2 $\mathrm{mAh\,cm^{-2}}$ (Figure 6 f). Therein the Li metal fills the voids between TA-ZIF-67 particles, enabling a comparatively dense cross section without long Li dendrites. Note that some short Li nanosheets are vertically squeezed out of the compact cross section (Figure 6g). The potential catalysis of Co-based capsules is likely responsible for the formation of nanostructured Li arrays.[41] After 40 cycles (Figure 6h and i), the texture of cross section is still compact. The nanostructures of Li do not grow and they in turn are electrochemically melted into monolithic grains after long-term cycling. In contrast, the Cu substrate leads to the wrinkled and rough surface of Li plating with irregular "dead" Li formation and deteriorated Li dendrite growth after 40 cycles (Figure S19). Crucially, the stuffed Li inside capsule and planted Li at capsule surface are clearly observed in TEM image (Figure 6j). This translucent Li species disappears under the irradiation of high energy e-beam. And the whole particle, especially the region around inner NPs, becomes bright under irradiation (Figure 6k). It means that the Li metal distributed around NPs has been sublimated, further proving the validity of seeding-induced Li nucleation/growth mode.

Benefiting from the synergistic effect of low-barrier nucleation and high-efficiency encapsulation of Li metal, the seed-contained hollow hosts also enable the performance improvement of Li/$\mathrm{LiFePO_4}$ full cells. Prior to cycling, the c-Au@ZIF-8 and TA-ZIF-67 electrodes are preloaded with 5 $\mathrm{mAh\,cm^{-2}}$ Li as anodes. The pristine Li foil is directly used as control anode. The full cell based on lithiated c-Au@ZIF-8 delivers a high discharge capacity of 143 $\mathrm{mAh\,g^{-1}}$ at 0.5 C (Figure 7a), whereas that of control cell is only 124 $\mathrm{mAh\,g^{-1}}$. With the progress of cycling, the control cell suffers from rapid capacity degradation with capacities of 100, 71, 52 and 46 $\mathrm{mAh\,g^{-1}}$ after 50, 100, 150 and 200 cycles, respectively (Figure S20). However, the modified cell displays much better capacity preservation with 115, 107.3, 107 and 103 $\mathrm{mAh\,g^{-1}}$ after 50, 100, 150 and 200 cycles, respectively (Figure 7b). The full cell with TA-ZIF-67 host also enables the high reversible capacities of 139 and 96 $\mathrm{mAh\,g^{-1}}$ after 100 and 200 cycles, respectively (Figure 7c and d). Moreover, both the modified cells show constantly higher and more stable CEs over 99.5 %, compared with the fluctuating CEs in control cell. Note that the low CEs (80–90 %) for control cell during the initial cycles reflect that the naked Li undergoes substantial side reaction with electrolyte, resulting in the formation of dendritic and dead Li. The more stable Li plating/stripping in lithiophilic hollow structure (c-Au@ZIF-8 or TA-ZIF-67) significantly enhances Li ultilization even under the lean Li condition (Figure S21), leading to the much better capacity retention in modified cells. Their higher capacity and reversibility reconfirm the synergistic effect of alloying/conversion nanoseeds (Au and Co-O) and 3D hollow structure. We also performed the electrochemical tests of symmetrical cells and full cells based on separated pure Au and carbon shell electrodes (Figure S22). These full cells deliver the lower and fluctuant discharge capacities with inferior cycling stability compared

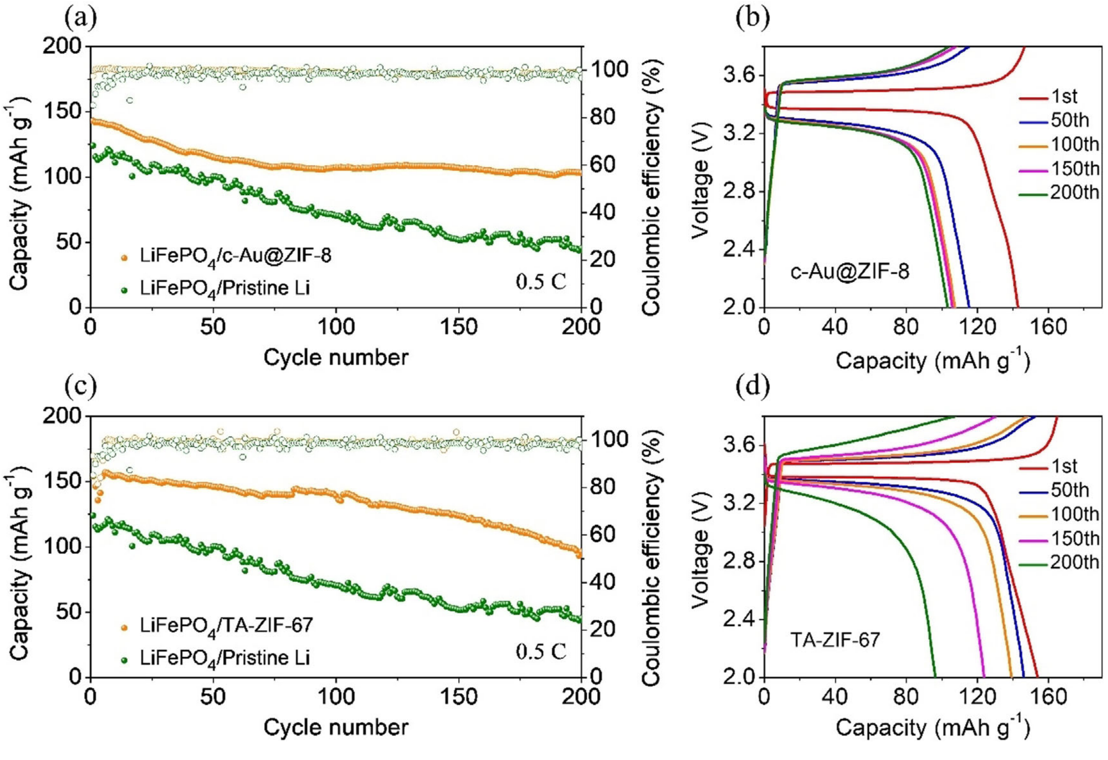

Figure 7. a) Galvanostatic cycling performance of Li/$\mathrm{LiFePO_4}$ cells based on lithiated c-Au@ZIF-8 and pristine Li-metal anodes at 0.5 C. b) Corresponding voltage profiles of $\mathrm{LiFePO_4}$ cell based on lithiated c-Au@ZIF-8 anode at different cycle stages. c) Cycling performance comparison of Li/$\mathrm{LiFePO_4}$ cells with lithiated TA-ZIF-67 and pristine Li-metal anodes at 0.5 C. d) Discharge-charge curves of $\mathrm{LiFePO_4}$ cell coupled with lithiated TA-ZIF-67 anode at different cycle stages.

with the case of c-Au@ZIF-8, and these symmetric cells experience much quicker cycling degradation. These comparisons emphasize the advantage of the combination of carbon shell and lithiophilic Au seeds.

The density functional theory (DFT) calculation was conducted to determine the binding energy (E_b) between Li and nanoseeds. Taking the Au NPs as an example, the E_b value of Li atom on Au (111) is −3.08 eV, which is more negative than that of Cu (111) (−2.59 eV, Figure S23). The binding energy exceeding 3 eV is considerably high to endow superior lithiophilicity. Note that Li is body-centered cubic, whereas Au and Cu are face-centered cubic. Since the (111) planes for the latters have the largest planar density and it is the (110) plane for the former, the atomic distance is calculated based on these crystal planes. The length of two atoms along the Li (110) crystallographic plane is 4.96 Å, matching well with that (4.99 Å) along Au (111) plane (Figure S23c–e). However the length of Cu atoms along (111) plane is 4.43 Å. Therefore the lattice mismatch between Li and Au is just 0.6%, much smaller than that between Li and Cu (12.9%). The in-plane matching may induce an aligned growth of Li on Au as indicated from the appearance of island-like grown Li columns on the surface of c-Au@ZIF-8 (Figure 3i and j). In order to better observe the Li deposition on Au, an Au layer was deposited on Cu by sputtering as current collector, which was then loaded with 2 mAh cm^{-2} Li (Figure S24). We can find that the Li metal can penetrate into the gaps between Au particles, and completely envelope each Au particles, which induce the columnar extrusion of Li deposit. In our capsule host, the Au NPs are much smaller and more discrete, therefore leading to the appearance of island-like distribution (i.e. nano-columnar-structure) of Li grown from these Au seeds. Moreover, these Au NPs not only can react with Li to form Li_xAu alloy, but also can dissolve into Li (ca. 0.7 at%) to form a solid solution layer as buffer layer to eliminate the nucleation barrier (Figure S1).[30] However, Li metal neither forms an alloy with Cu nor dissolves in Cu at ambience temperature. As a result, Li metal would preferentially adsorb and deposit on the surface of inbuilt NPs (Au and cobalt oxide). Such lithiophilic NPs behave like nucleation seeds to guide Li deposition through forming alloy (composite) phase as buffer layer to overcome nucleation barrier. The interconnected porous framework further confines the expansion of Li metal and flourishing of Li dendrites. The combination of spatial confinement and seeding-induced nucleation significantly reinforces the advantages of these two strategies.

Conclusion

We propose a dual modulation mode of consecutive nucleation and confinement towards Li plating via lithiophilic hollow host frameworks with internal decoration of Au or cobalt oxide NPs, which were prepared by TA-etching MOF. These NPs can act as heterogeneous seeds for zero-overpotential nucleation, and promote the inward injection of Li metal in the host cavities and then the conformal coating of Li on the outer surface of host during plating. These effects are well monitored by SEM and TEM imaging. This modulation alleviates the dendrite growth and volume expansion of Li plating. The interconnected porous network of host obviously enhances the cycling and rate performances of metallic Li anode, enabling a much longer lifespan over 1200 h for c-Au@ZIF-8 based symmetric cells with low overpotential (ca. 20 mV). For Li/Cu asymmetric cells, both the c-Au@ZIF-8 and TA-ZIF-67 electrodes can tolerate a high current density of 10 mA cm^{-2} for 220 and 150 cycles, respectively. These lithiophilic 3D hosts are also successfully applied in $LiFePO_4$ full cells with much better cycling stability. This study heightens the integration of consecutive nucleation and confinement modulation towards durable Li-metal anode.

Acknowledgements

This work was supported by NSAF (Grant No. U1830113), National Natural Science Foundation of China (51772313 and 21975276), National Key R&D Program of China (2016YFB0901600), and Shanghai Science and Technology Committee (20520710800).

Conflict of interest

The authors declare no conflict of interest.

Keywords: 3D hollow structures · Li dendrite inhibition · Li metal batteries · seeding-induced deposition · spatial confinement

---

[1] H. Kim, G. Jeong, Y.-U. Kim, J.-H. Kim, C.-M. Park, H.-J. Sohn, *Chem. Soc. Rev.* **2013**, *42*, 9011.
[2] B. Liu, J.-G. Zhang, W. Xu, *Joule* **2018**, *2*, 833.
[3] Q. Yang, M. Cui, J. Hu, F. Chu, Y. Zheng, J. Liu, C. Li, *ACS Nano* **2020**, *14*, 1866.
[4] K. Zhang, G.-H. Lee, M. Park, W. Li, Y.-M. Kang, *Adv. Energy Mater.* **2016**, *6*, 1600811.
[5] K. N. Wood, M. Noked, N. P. Dasgupta, *ACS Energy Lett.* **2017**, *2*, 664.
[6] R. Zhang, X.-R. Chen, X. Chen, X.-B. Cheng, X.-Q. Zhang, C. Yan, Q. Zhang, *Angew. Chem. Int. Ed.* **2017**, *56*, 7764; *Angew. Chem.* **2017**, *129*, 7872.
[7] J. Meng, F. Chu, J. Hu, C. Li, *Adv. Funct. Mater.* **2019**, *29*, 190220.
[8] D. Lin, Y. Liu, Z. Liang, H.-W. Lee, J. Sun, H. Wang, K. Yan, J. Xie, Y. Cui, *Nat. Nanotechnol.* **2016**, *11*, 626.
[9] S. Wu, Z. Zhang, M. Lan, S. Yang, J. Cheng, J. Cai, J. Shen, Y. Zhu, K. Zhang, W. Zhang, *Adv. Mater.* **2018**, *30*, 1705830.
[10] H. Wu, Q. Wu, F. Chu, J. Hu, Y. Cui, C. Yin, C. Li, *J. Power Sources* **2019**, *419*, 72.
[11] X.-B. Cheng, R. Zhang, C.-Z. Zhao, Q. Zhang, *Chem. Rev.* **2017**, *117*, 10403.
[12] W. Li, H. Yao, K. Yan, G. Zheng, Z. Liang, Y.-M. Chiang, Y. Cui, *Nat. Commun.* **2015**, *6*, 7436.
[13] F. Chu, J. Hu, C. Wu, Z. Yao, J. Tian, Z. Li, C. Li, *ACS Appl. Mater. Interfaces* **2019**, *11*, 3869.
[14] F. Ding, W. Xu, G. L. Graff, J. Zhang, M. L. Sushko, X. Chen, Y. Shao, M. H. Engelhard, Z. Nie, J. Xiao, X. Liu, P. V. Sushko, J. Liu, J.-G. Zhang, *J. Am. Chem. Soc.* **2013**, *135*, 4450.
[15] Y. Lu, Z. Tu, L. A. Archer, *Nat. Mater.* **2014**, *13*, 961.

[16] H. Yu, J. Zhao, L. Ben, Y. Zhan, Y. Wu, X. Huang, *ACS Energy Lett.* **2017**, *2*, 1296.
[17] G. Zheng, S. W. Lee, Z. Liang, H.-W. Lee, K. Yan, H. Yao, H. Wang, W. Li, S. Chu, Y. Cui, *Nat. Nanotechnol.* **2014**, *9*, 618.
[18] M. Bai, K. Xie, K. Yuan, K. Zhang, N. Li, C. Shen, Y. Lai, R. Vajtai, P. Ajayan, B. Wei, *Adv. Mater.* **2018**, *30*, 1801213.
[19] K. Yan, H.-W. Lee, T. Gao, G. Zheng, H. Yao, H. Wang, Z. Lu, Y. Zhou, Z. Liang, Z. Liu, S. Chu, Y. Cui, *Nano Lett.* **2014**, *14*, 6016.
[20] C.-P. Yang, Y.-X. Yin, S.-F. Zhang, N.-W. Li, Y.-G. Guo, *Nat. Commun.* **2015**, *6*, 8058.
[21] L.-L. Lu, Y. Zhang, Z. Pan, H.-B. Yao, F. Zhou, S.-H. Yu, *Energy Storage Mater.* **2017**, *9*, 31.
[22] T.-T. Zuo, X.-W. Wu, C.-P. Yang, Y.-X. Yin, H. Ye, N.-W. Li, Y.-G. Guo, *Adv. Mater.* **2017**, *29*, 1700389.
[23] Y. Zhang, J. Meng, K. Chen, H. Wu, J. Hu, C. Li, *ACS Energy Lett.* **2020**, *5*, 1167.
[24] X. Han, Y. Gong, K. Fu, X. He, G. T. Hitz, J. Dai, A. Pearse, B. Liu, H. Wang, G. Rubloff, Y. Mo, V. Thangadurai, E. D. Wachsman, L. Hu, *Nat. Mater.* **2017**, *16*, 572.
[25] Z. Wan, D. Lei, W. Yang, C. Liu, K. Shi, X. Hao, L. Shen, W. Lv, B. Li, Q. H. Yang, F. Kang, Y. B. He, *Adv. Funct. Mater.* **2019**, *29*, 1805301.
[26] J. Meng, Y. Zhang, X. Zhou, M. Lei, C. Li, *Nat. Commun.* **2020**, *11*, 3716.
[27] M. Zhu, B. Li, S. Li, Z. Du, Y. Gong, S. Yang, *Adv. Energy Mater.* **2018**, *8*, 1703505.
[28] C. Yang, Y. Yao, S. He, H. Xie, E. Hitz, L. Hu, *Adv. Mater.* **2017**, *29*, 1702714.
[29] Q. Li, S. Zhu, Y. Lu, *Adv. Funct. Mater.* **2017**, *27*, 1606422.
[30] K. Yan, Z. Lu, H.-W. Lee, F. Xiong, P.-C. Hsu, Y. Li, J. Zhao, S. Chu, Y. Cui, *Nat. Energy* **2016**, *1*, 16010.
[31] J. Yang, F. Zhao, B. Zeng, *RSC Adv.* **2016**, *6*, 23403.
[32] L. Chen, Y. Peng, H. Wang, Z. Gu, C. Duan, *Chem. Commun.* **2014**, *50*, 8651.
[33] M. Hu, Y. Ju, K. Liang, T. Suma, J. Cui, F. Caruso, *Adv. Funct. Mater.* **2016**, *26*, 5827.
[34] H. Wang, W. Zhu, Y. Ping, C. Wang, N. Gao, X. Yin, C. Gu, D. Ding, C. J. Brinker, G. Li, *ACS Appl. Mater. Interfaces* **2017**, *9*, 14258.
[35] Z. Ye, S. Wu, C. Zheng, L. Yang, P. Zhang, Z. Zhang, *Langmuir* **2017**, *33*, 12952.
[36] Z.-X. Cai, Z.-L. Wang, J. Kim, Y. Yamauchi, *Adv. Mater.* **2019**, *31*, 1804903.
[37] H. Yang, S. J. Bradley, A. Chan, G. I. N. Waterhouse, T. Nann, P. E. Kruger, S. G. Telfer, *J. Am. Chem. Soc.* **2016**, *138*, 11872.
[38] D. Borissov, A. Pareek, F. U. Renner, M. Rohwerder, *Phys. Chem. Chem. Phys.* **2010**, *12*, 2059.
[39] L. Liu, Y.-X. Yin, J.-Y. Li, S.-H. Wang, Y.-G. Guo, L.-J. Wan, *Adv. Mater.* **2018**, *30*, 1706216.
[40] W. Zhang, H. L. Zhuang, L. Fan, L. Gao, Y. Lu, *Sci. Adv.* **2018**, *4*, eaar4410.
[41] M. Huang, Z. Yao, Q. Wu, Y. Zheng, J. Liu, C. Li, *ACS Appl. Mater. Interfaces* **2020**, *12*, 46132.
[42] L. Wang, X. Zhu, Y. Guan, J. Zhang, F. Ai, W. Zhang, Y. Xiang, S. Vijiayan, G. Li, Y. Huang, G. Cao, Y. Yang, H. Zhang, *Energy Storage Mater.* **2018**, *11*, 191.
[43] X. Zhou, J. Tian, J. Hu, C. Lin, *Adv. Mater.* **2018**, *30*, 1704166.
[44] C. Avci, J. Ariñez-Soriano, A. Carné-Sánchez, V. Guillerm, C. Carbonell, I. Imaz, D. Maspoch, *Angew. Chem. Int. Ed.* **2015**, *54*, 14417; *Angew. Chem.* **2015**, *127*, 14625.
[45] W. Zhang, X. Jiang, X. Wang, Y. V. Kaneti, Y. Chen, J. Liu, J.-S. Jiang, Y. Yamauchi, M. Hu, *Angew. Chem. Int. Ed.* **2017**, *56*, 8435; *Angew. Chem.* **2017**, *129*, 8555.
[46] C. Zhang, S. Wei, Y. Hu, H. Tang, J. Gao, Z. Yin, Q. Guan, *J. Colloid Interface Sci.* **2018**, *512*, 55.
[47] X. Ge, C. Li, Z. Li, L. Yin, *Electrochim. Acta* **2018**, *281*, 700.
[48] M. Zhang, Q. Dai, H. Zheng, M. Chen, L. Dai, *Adv. Mater.* **2018**, *30*, 1705431.
[49] P. Wang, J. Tian, J. Hu, X. Zhou, C. Li, *ACS Nano* **2017**, *11*, 7390.
[50] H. Jing, X. Song, S. Ren, Y. Shi, Y. An, Y. Yang, M. Feng, S. Ma, C. Hao, *Electrochim. Acta* **2016**, *213*, 252.
[51] H. Zhong, Y. Luo, S. He, P. Tang, D. Li, N. Alonso-Vante, Y. Feng, *ACS Appl. Mater. Interfaces* **2017**, *9*, 2541.
[52] X. Li, Q. Jiang, S. Dou, L. Deng, J. Huo, S. Wang, *J. Mater. Chem. A* **2016**, *4*, 15836.

Manuscript received: February 19, 2021
Revised manuscript received: April 2, 2021
Accepted manuscript online: April 10, 2021
Version of record online: ■■ ■■, ■■■■

Research Articles

Batteries

M. Huang, Z. Yao, Q. Yang, C. Li* ▮▮▮▮–▮▮▮▮

Consecutive Nucleation and Confinement Modulation towards Li Plating in Seeded Capsules for Durable Li-Metal Batteries

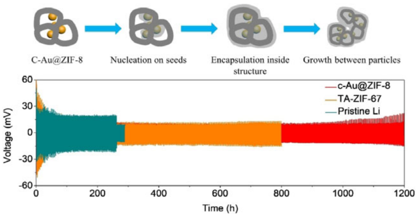

A dual modulation strategy of consecutive nucleation and confined growth of Li metal is proposed by using the metal–organic framework (MOF) derivative hollow capsule with inbuilt lithiophilic Au or Co-O nanoparticle (NP) seeds as heterogeneous host.